JOURNAL OF GEOPHYSICAL RESEARCH, VOL. 111, B08405, doi:10.1029/2006JB004258, 2006

An aseismic slip pulse in northern Chile and along-strike variations in seismogenic behavior

M. E. Pritchard[1] and M. Simons[2]

Received 2 January 2006; revised 6 April 2006; accepted 12 May 2006; published 19 August 2006.

[1] We use interferometric synthetic aperture radar, GPS, and seismic observations spanning 5 to 18 years to reveal a detailed kinematic picture of the spatiotemporal evolution of fault slip in a region corresponding to the 30 July 1995 M_w 8.1 subduction zone megathrust earthquake in northern Chile. In a single area, we document a complex mosaic of phenomena including large earthquakes, postseismic afterslip with a spatial distribution that appears to be tied to variations in coastal morphology, and a completely aseismic pulse that may have triggered a M_w 7.1 earthquake on 30 January 1998. In contrast to simple models of fault slip behavior, this spatial heterogeneity indicates that frictional parameters on the fault do not have a systematic transition with depth and also vary rapidly along strike. The low amount of afterslip from the M_w 8.1 earthquake relative to other similar events suggests that postseismic behavior may be modulated by the amount of sediment subducted.

Citation: Pritchard, M. E., and M. Simons (2006), An aseismic slip pulse in northern Chile and along-strike variations in seismogenic behavior, *J. Geophys. Res.*, *111*, B08405, doi:10.1029/2006JB004258.

1. Introduction

[2] Large shallow thrust earthquakes are found within a narrow range of depths in subduction zones and do not occur in all areas of subduction [*Kanamori*, 1986]. While large-scale features of each subduction zone (temperature and/or normal tractions on the plate interface [e.g., *Kanamori*, 1986; *Scholz and Campos*, 1995]) are thought to govern the along-strike and depth distribution of these large earthquakes, several observations in various locations indicate that smaller-scale variations in frictional properties on the plate interface are of equal or greater importance [*Pacheco et al.*, 1993; *Song and Simons*, 2003; *Wells et al.*, 2003].

[3] To better understand these along-strike variations in seismogenic behavior, we compare the detailed slip distribution during the M_w 8.1 Antofagasta, Chile, earthquake on 30 July 1995 (hereafter called the 1995 earthquake), its large aftershocks (six earthquakes with $M_w > 6$), and the postseismic afterslip following these events (Figures 1 and 2). The 1995 main shock filled a seismic gap in the Nazca–South American subduction zone between areas that ruptured in 1877 and 1922 (Figures 1 and 2). The fault slip during the 1995 earthquake has been constrained by several workers using teleseismic, Global Positioning System (GPS) and interferometric synthetic aperture radar (InSAR) data [e.g., *Ruegg et al.*, 1996; *Ihmlé and Ruegg*, 1997; *Delouis et al.*, 1997; *Klotz et al.*, 1999; *Pritchard et al.*, 2006]. The deformation from the largest aftershocks in 1998 (M_w 7.1) and 1996 (M_w 6.7, see Figure 1) have been studied by teleseismic, GPS, and InSAR data [*Pritchard et al.*, 2006], and the four other aftershocks with $M_w > 6$ have been located with seismic data [*Delouis et al.*, 1997; *Pritchard et al.*, 2006].

[4] Previous work has documented the existence of postseismic deformation following the 1995 main shock [e.g., *Klotz et al.*, 2001; *Khazaradze and Klotz*, 2003; *Xia et al.*, 2003; *Chlieh et al.*, 2004]. We extend these studies by combining InSAR as well as campaign and continuous GPS observations to constrain the detailed spatiotemporal evolution of aseismic slip. Such kinematic maps of the spatiotemporal evolution of fault slip can be used to test dynamical models of afterslip [e.g., *Hearn et al.*, 2002; *Miyazaki et al.*, 2004; *Montési*, 2004] which assess the mechanisms of postseismic creep (frictional, viscoelastic, poroelastic, etc.), the relative importance of spatial variations of material properties, and the importance of tectonic loading. Of particular interest in studying the underlying mechanics of this deformation is constraining the relative location of coseismic and postseismic slip [e.g., *Marone*, 1998], and documenting the location and spatiotemporal evolution of aseismic pulses of deformation [e.g., *Liu and Rice*, 2005]. Here, we document small-scale complexity of slip behavior including aseismic transients within a relatively small segment of a single subducting zone, and show that this complexity appears to be independent of obvious structural features on the subducting plate.

2. Data Used

[5] Combining the InSAR and GPS data is desirable for several reasons. Individual GPS measurements are more

[1]Department of Earth and Atmospheric Sciences, Cornell University, Ithaca, New York, USA.
[2]Seismological Laboratory, Division of Geological and Planetary Sciences, California Institute of Technology, Pasadena, California, USA.

0148-0227/06/2006JB004258$09.00

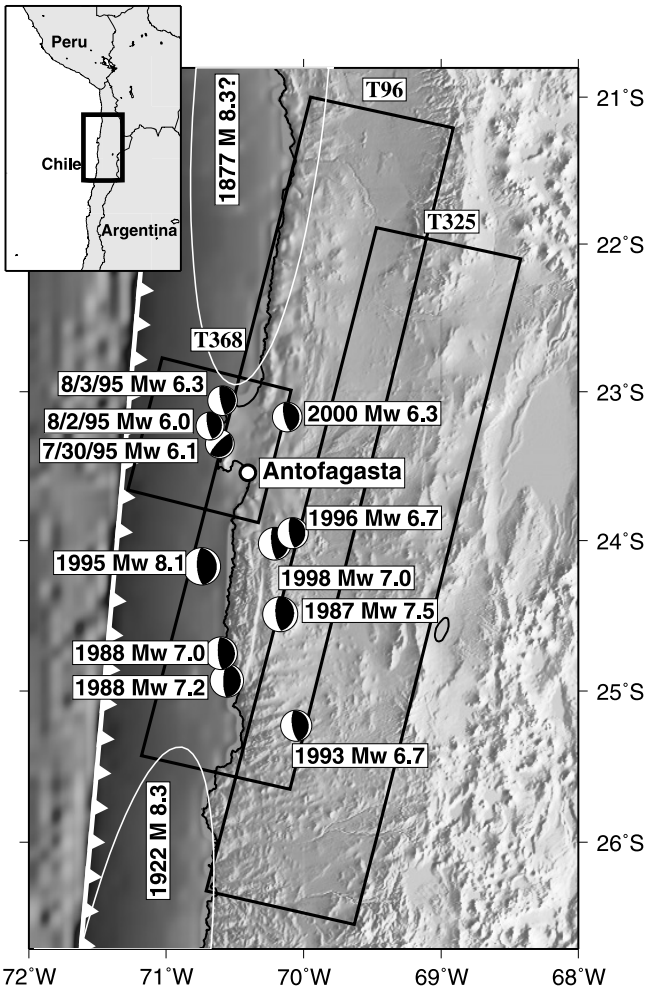

Figure 1. Locations of earthquakes with $M_w > 6$ that are presumed to have occurred on the fault interface between 1987 and 2000 in the study area (see inset map). The white circle is the city of Antofagasta. Mechanisms are from the Harvard centroid moment tensor (CMT) catalog, but locations are from the National Earthquake Information Center catalog, except for the 1995 M_w 8.1 event, which is from a local network [*Monfret et al.*, 1995]. Black rectangles show the outline of radar coverage used in this study (T96 is track 96, Table 1). The white ellipses show the approximate rupture areas of the largest earthquakes adjacent to our study area. The size and spatial extent of the 1877 rupture is especially uncertain, [e.g., *Comte and Pardo*, 1991; *Beck et al.*, 1998].

accurate than individual InSAR observations, and the GPS observations record more than one component of deformation. However, there are several large spatial and temporal gaps in the GPS coverage. The published GPS velocities (with the exception of the 30 days of data from the continuous station) record the horizontal deformation, while the available InSAR observations contain mostly vertical deformation. In addition, the two data types are complementary in that they do not suffer from the same types of errors.

2.1. InSAR Data

[6] We process data from the ERS-1 and ERS-2 satellites (Table 1 and Figure 3) using the publicly available ROI_-PAC software [*Rosen et al.*, 2004] and the 90-m posting digital elevation model (DEM) from the Shuttle Radar Topography Mission (SRTM) [*Farr and Kobrick*, 2000]. We subsample the interferograms with a sampling density proportional to the curvature of the displacement field, to reduce the number of points from millions to hundreds or thousands [*Simons et al.*, 2002]. Further details on the InSAR method and processing procedures are available from *Rosen et al.* [2000] and *Pritchard et al.* [2002].

[7] Because of uncertainties in the quality of the orbital ephemeris, we estimate interferometric baselines empirically. We calculate the baseline parameters (e.g., horizontal and

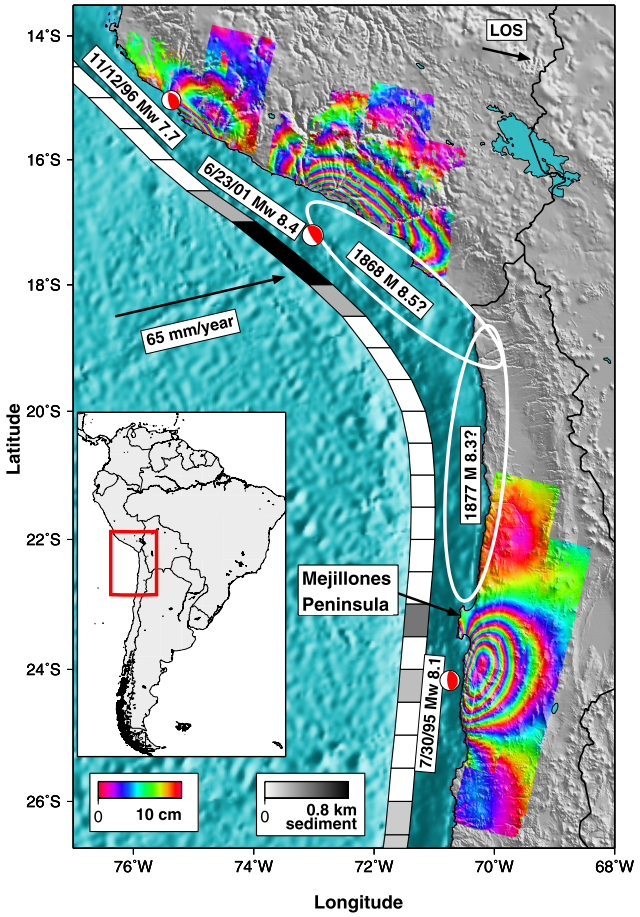

Figure 2. A compilation of ERS interferograms for three earthquakes on the subduction megathrust [*Pritchard*, 2003]. The color contours of the line-of-sight (LOS) component of ground deformation are draped over shaded relief and bathymetry. The approximate LOS between the ground and the satellite is shown by the labeled arrow. The Harvard CMT mechanisms for the three large earthquakes are also shown. White ellipses and associated labels indicate the region of the Arica gap (between the 1995 and 2001 earthquakes that has not slipped in the last century) [*Comte and Pardo*, 1991], and black lines show political borders. The relative Nazca–South American convergence direction is shown by the black arrow (~65 mm/yr) [*Angermann et al.*, 1999]. The gray shaded boxes show the maximum amount of trench sediment in every 0.5° interval [*Schweller et al.*, 1981].

Table 1. Interferograms Used to Constrain Postseismic Deformation in Northern Chile[a]

Track[b]	Frame(s)	Image 1	Image 2	$B_\perp$, m
96	4059–4113	30 Jul 1995	12 Oct 1997	110
96	4059–4113	30 Jul 1995	13 Oct 1997	220
96	4059–4113	30 Jul 1995	8 Oct 1995	300
96	4059–4113	30 Jul 1995	31 Mar 1996	320
96	4059–4113	8 Oct 1995	13 Oct 1997	80
96	4059–4113	31 Mar 1996	2 Dec 1996	130
96	4059–4113	31 Mar 1996	21 Apr 1997	90
96	4059–4113	31 Mar 1996	17 Nov 1997	250
96	4059–4113	1 Apr 1996	21 Apr 1997	30
96	4059–4113	1 Apr 1996	17 Nov 1997	130
96	4059–4113	2 Dec 1996	21 Apr 1997	40
96	4059–4113	2 Dec 1996	17 Nov 1997	120
96	4059–4113	21 Apr 1997	12 Oct 1997	400
96	4059–4113	21 Apr 1997	17 Nov 1997	160
368	4077	18 Aug 1995	22 Sep 1995	180
368	4077	18 Aug 1995	24 May 1996	150
368	4077	22 Sep 1995	24 May 1996	330
368	4077	18 Aug. 1995	25 May 1996	250
368	4077	22 Sep 1995	21 Dec 1996	2
368	4077	18 Aug 1995	21 Dec 1996	180
325	4059–4131	15 Aug 1995	19 Sep 1995	30
325	4059–4131	19 Sep 1995	21 May 1996	10
325	4059–4131	15 Aug 1995	21 May 1996	30
325	4059–4131	19 Sep 1995	22 May 1996	80
325	4059–4131	15 Aug 1995	22 May 1996	110
96	4059–4113	31 Mar 1996	7 Dec 1998	100
96	4059–4113	1 Apr 1996	7 Dec 1998	200
96	4059–4113	21 Apr 1997	7 Dec 1998	190
96	4059–4113	13 Oct 1997	8 Aug 1999	90
96	4059–4113	17 Nov 1997	6 Mar 2000	260
96	4059–4113	21 Apr 1997	6 Mar 2000	110
96	4059–4113	13 Oct. 1997	31 May 1999	90
96	4059–4113	12 Oct 1997	7 Dec 1998	120
368	4077	19 Apr 1996	10 Apr 1999	50
368	4077	21 Dec 1996	26 Dec 1998	50
96	4059–4113	7 Dec 1998	6 Mar 2000	80

[a] $B_\perp$ is the perpendicular baseline between the two satellite images used to make the interferogram, and a larger $B_\perp$ means that the interferogram is more sensitive to errors in removing the effects of topographic relief [e.g., *Rosen et al.*, 2000]. The time spans of the interferograms relative to each other and the GPS data are shown graphically in Figure 3.

[b] See Figure 1 for the location of the satellite tracks.

vertical baselines plus quadratic baseline variations as a function of range and azimuth [*Pritchard et al.*, 2002]) that minimize the phase difference between the interferogram and a synthetic interferogram made with the SRTM DEM [*Rosen et al.*, 1996]. This process assumes that the deformation signal is small (justified below). Only a portion of the deformation field is on land, and coupled with the long-wavelength of surface deformation caused by the afterslip, a real deformation signal can look similar to long-wavelength artifacts caused by errors in the orbits [e.g., *Zebker et al.*, 1994]. To correct for this ambiguity when solving for fault slip, we simultaneously invert for six parameters that include an absolute offset for the InSAR displacement data as well as linear and quadratic variations in space for each interferogram. These parameters account for errors in our empirical estimation of quadratic baseline parameters, and are hereafter called ''ramp'' parameters.

[8] The InSAR data provides more temporal coverage than the GPS data, but the data are noisier. In particular, in parts of the interferograms, the phase is correlated with topography (Figure 4). This is not an error in the removal of topography from the interferogram, but is likely due to variations in the troposphere between acquisition of SAR images [e.g., *Beauducel et al.*, 2000]. We attempt to account for this contamination by determining a single linear function per interferogram that best relates the phase signal to

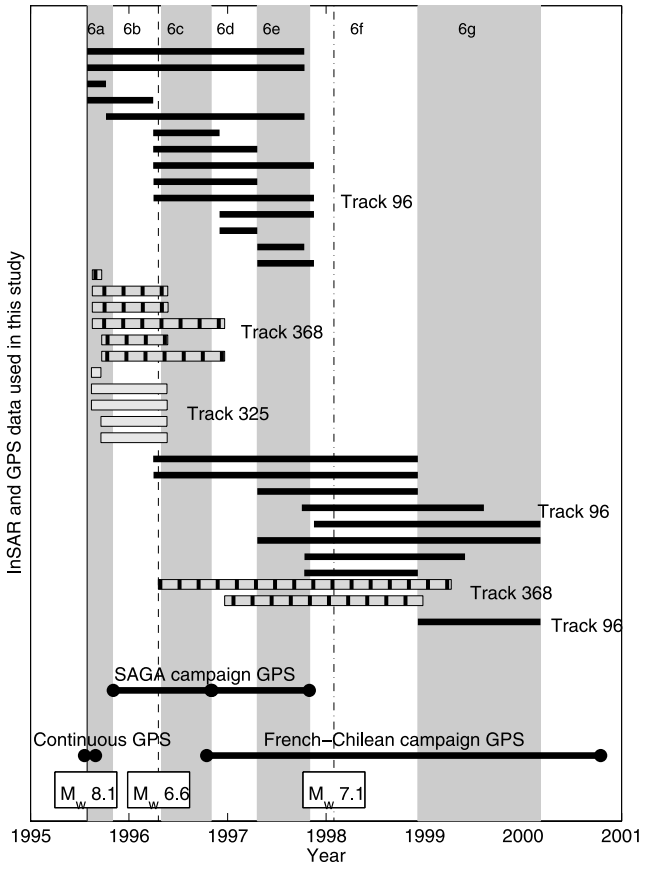

Figure 3. Time spans of geodetic data in northern Chile. Dates for InSAR images are listed in Table 1. Each different track of InSAR data is shown as a different symbol. There are three campaigns of GPS data: 3 to 15 months postseismic [*Klotz et al.*, 2001]; the second year postseismic (15 to 27 months postseismic) [*Khazaradze and Klotz*, 2003]; and between October 1996 and October 2000 (15 to 63 months postseismic) [*Chlieh et al.*, 2004]. Continuous GPS measurements are from a single station in Antofagasta [*Melbourne et al.*, 2002]. The alternating gray and white columns labeled 6a, 6b, etc., correspond to the temporal subdomains adopted in this study. The slip in each subdomain is shown in the corresponding frames of Figure 6 text, e.g., fault slip during the time interval spanned by 6a is shown in Figure 6a. We remove models of deformation from the 1996 (M_w 6.7) and 1998 (M_w 7.1) earthquakes [*Pritchard*, 2003; *Pritchard et al.*, 2006] from the InSAR and GPS data. It is possible that our models for the 1996 and 1998 earthquakes include some postseismic deformation (because the InSAR data spans many months/years), but these effects are small based on noncoseismic interferograms and because our coseismic models for these earthquakes are also constrained by seismic data. We also remove the effects of interseismic deformation during the time periods [*Bevis et al.*, 2001; *Khazaradze and Klotz*, 2003; *Chlieh et al.*, 2004].

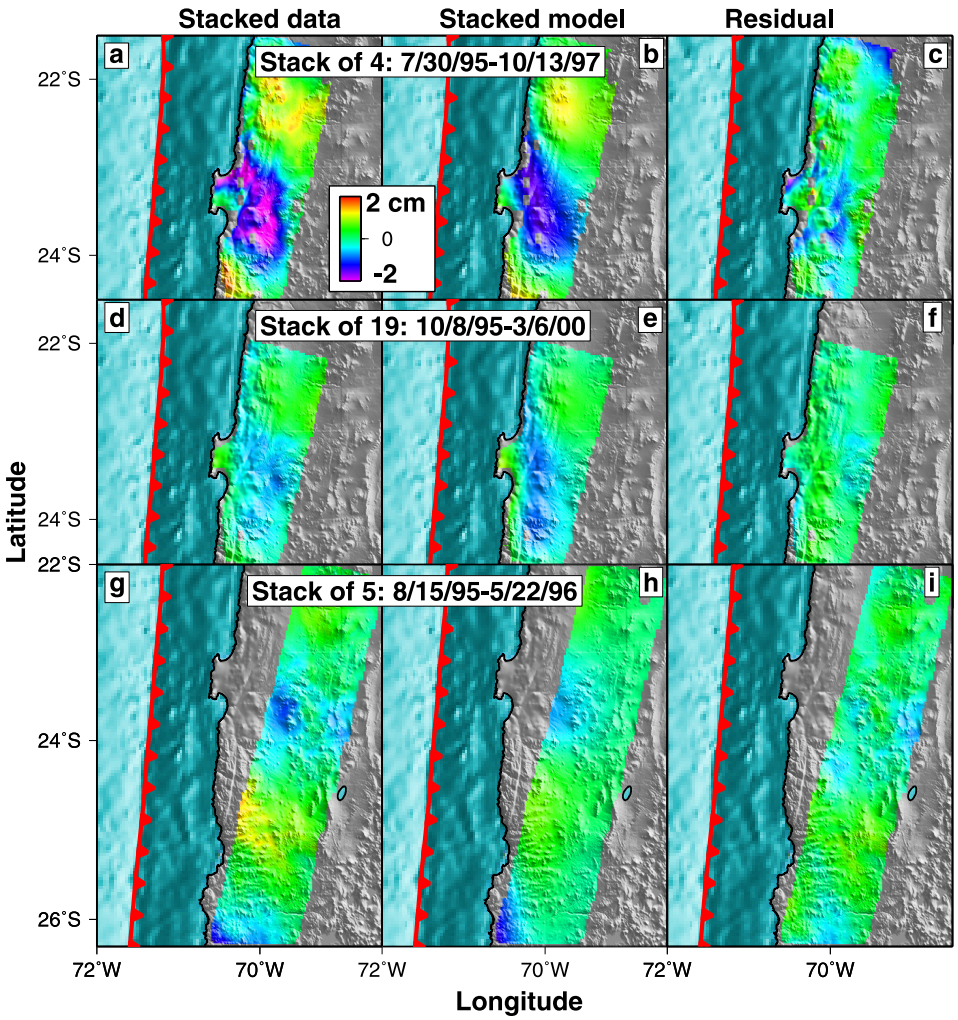

Figure 4. Stacked InSAR observations of postseismic deformation. (a) Stack of four interferograms made using the image acquired on 30 July 1995 (9.5 hours after the earthquake). The broadscale signal (up-down-up, from north to south) is consistent with regional long-wavelength topography. Some of the deformation on the peninsula itself (particularly the north-south gradient) might be related to $M_w \sim 6$ aftershocks [*Pritchard et al.*, 2006]. (b) Sum of all modeled postseismic deformation during the appropriate temporal subdomains for the same interferograms. (c) Residual after removal of the model prediction from the data. (d) Stack of the 19 other postseismic interferograms from track 96, with the models of 1996 (M_w 6.7) and 1998 (M_w 7.1) earthquakes removed where appropriate [*Pritchard et al.*, 2006]. (e) Stacked models of the 19 interferograms. (f) Residual after removal of the model prediction from the data. (g) Stack of five interferograms from track 325 (with the model of the 1996 M_w 6.7 earthquake removed). The sign of the deformation in this track is the same as in track 96. (h) Stack of the models from track 325. (i) Residual after removal of the model prediction from the data.

the topography. However, this correction has little effect, because the horizontal variations are of equal or more importance than the vertical variations. We do not attempt to account for such horizontal variations. Large horizontal variations are expected because of variations in water vapor content (e.g., correlated with distance to the coast).

[9] Postseismic deformation is barely above the detection limit for the available individual interferograms but is clear when the data are stacked from two independent satellite tracks, especially in stacks that include the radar image acquired 9.5 hours after the earthquake (Figure 4) [*Xia et al.*, 2003; *Chlieh et al.*, 2004]. Most of the surface deformation occurs north of the primary rupture area of the 1995 earthquake (inland of the Mejillones Peninsula) in the months following the earthquake. There is no clear transient deformation following a M_w 7.1 earthquake in 1998, but it is impossible to separate coseismic deformation from any rapid postseismic deformation that occurred during the first 10 months after the event.

2.2. Campaign and Continuous GPS Data

[10] The campaign GPS data [*Klotz et al.*, 2001; *Khazaradze and Klotz*, 2003; *Chlieh et al.*, 2004] reveal temporal variations in the deformation field (Figure 5), but observations are only available once a year or less frequently. Thus it is possible that the magnitude of deformation is

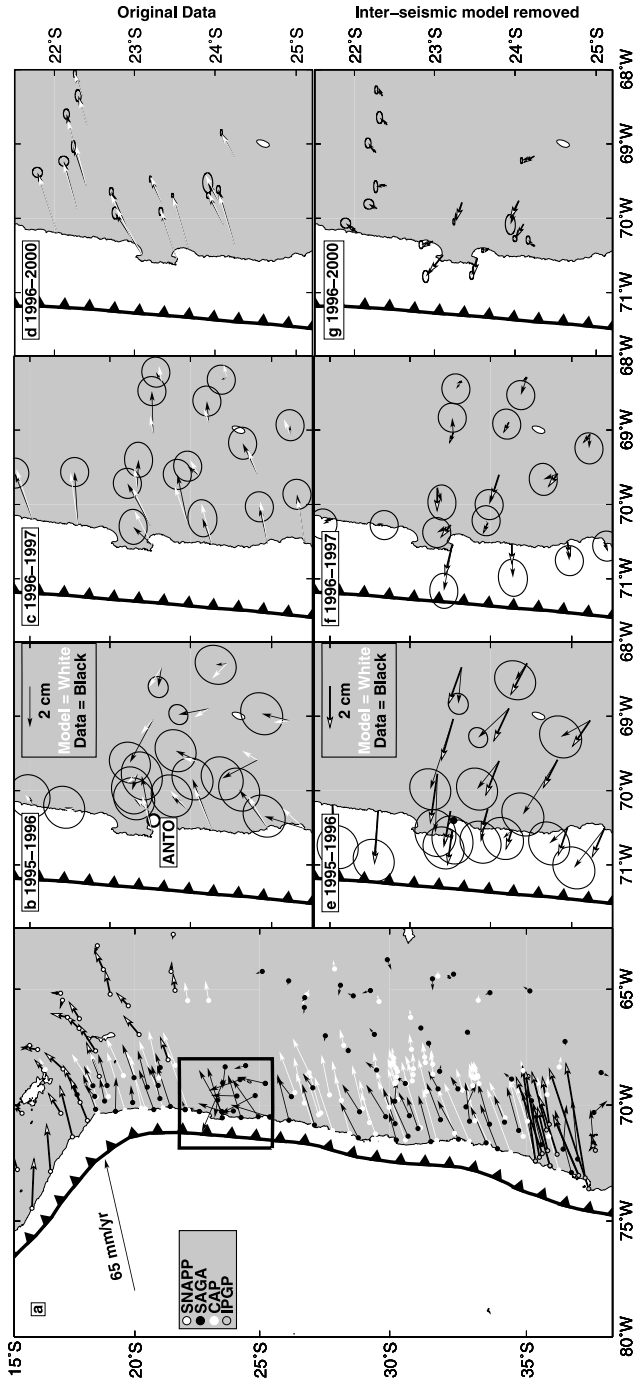

Figure 5. (a) Published velocities of GPS stations in South America relative to stable South America [*Angermann et al.*, 1999] from SNAPP [*Norabuena et al.*, 1998] (but with velocities from *Bevis et al.* [1999] and *Kendrick et al.* [2001] so that a common reference frame is used); CAP [*Kendrick et al.*, 1999; *Brooks et al.*, 2003]; SAGA [*Klotz et al.*, 2001; *Khazaradze and Klotz*, 2003]; and IPGP [*Ruegg et al.*, 2002; *Chlieh et al.*, 2004]. The error ellipses have been removed for the clarity of presentation. The relative Nazca–South American convergence rate and direction are shown by the black arrow [*Angermann et al.*, 1999], and the trench is shown by the black barbed line. The black box shows the region in Figures 5b–5g. (b) Black arrows showing the horizontal GPS postseismic deformation following the 1995 M_w 8.1 earthquake between 1996 and 1995, including the error ellipses (95% confidence) [*Klotz et al.*, 2001]. The white lines show the modeled displacements from our joint InSAR and GPS inversion for slip. The white circle shows the location of the continuous GPS station in Antofagasta (labeled ANTO, not to be confused with the continuous station ANTO in San Antonio, Texas). ANTO has only 30 days of data immediately after the earthquake, while the other stations show displacements over a 1-year period (Figure 3). (c) Observed [*Khazaradze and Klotz*, 2003] and predicted horizontal GPS postseismic deformation between 1996 and 1997 with same legend as in Figure 5a. (d) Observed [*Chlieh et al.*, 2004] and predicted horizontal GPS postseismic deformation between 1996 and 2000 with same legend as Figure 5a. (e–g) Same as Figures 5b–5d but with interseismic deformation removed (in this case, fully locked to 50 km depth [*Bevis et al.*, 2001]).

Table 2. Compilation of Rapid Postseismic Deformation in Subduction Zones Recorded by Geodetic Networks[a]

Earthquake	Coseismic Moment Magnitude	Postseismic (Fraction of Coseismic Moment)	Method	Seismic Coupling χ[b]	Rupture Depth/Bottom of Seismogenic Zone,[c] km	Sediment Thickness km
2005 Nias-Simeulue, Indonesia	8.7	>25% in 9 months[d]	GPS	0.007–0.6[e,f]	50[g]/35–55[h]	1.4–2[i,j]
2004 Sumatra-Andaman	9.0	30% in 45 days; 50% in 5 months[k]	GPS	0.007–0.6[e,f]	50[l]/35–55[h]	1.4–5[i,j]
2003 Tokachi-oki, Japan	8.0	40% in 30 days[m]	GPS	0.18–0.25[f]	40[m]/52–55[n]	0.3–0.8[i,j]
2001 Arequipa, Peru	8.4	20–40% in 1 year[o,p]	GPS/InSAR	0.16–0.86[e]	60[q]/50–60[r]	0.3–0.8[s]
1997 Kronotsky, Kamchatka	7.8	100% in 1–3 months[t]	GPS	0.49–1[f]	35[u]/38–43[n]	0.4[j]
1996 Nazca, Peru	7.7	<10% after first 60 days[q]	InSAR	0.16–0.86[e]	50[q]/50–60[r]	0[s]
1996 Hyuga-nada, Japan	2 quakes each 6.7	100% in ~1 year[v]	GPS	NA[w]	23[v]/20[x]	0.4[j]
1995 Jalisco, Mexico	8.0	47% in 5 months[p,y]	GPS	0.26–0.64[f]	20[y]/20–30[n]	0[z]
1995 Antofagasta, Chile	8.1	<20% in 1 year[p,aa,bb]	InSAR/GPS	0.01–0.84[e]	40[q]/40–50[n]	0–0.5[s]
1994 Sanriku-oki, Japan	7.7	>100% in 1 year[p,cc,dd]	GPS	0.18–0.25[f]	40[cc]/37–43[n]	0.3–0.8[i]
1992 Sanriku-oki, Japan	6.9	100% in 5 days[dd,ee]	strain-meter	0.18–0.33[f]	20[ff]/37–43[n]	0.3–0.8[i,j]
1989 Sanriku-oki, Japan	7.4	100% in 50 days[ee]	strain-meter	0.18–0.33[f]	40[ff]/37–43[n]	0.3–0.8[i,j]

[a]The time span referred to in column three is sometimes defined by the authors as time for "appreciable slip," while in other instances it refers to the decay time (time to 1/*e* of the initial value). We multiply the decay time by 5 (99.99% of the slip).
[b]Seismic coupling coefficient (see text).
[c]The bottom of a rupture is typically poorly resolved unless there is an extensive geodetic array, and even then estimates are accurate to only 5–10 km because of regularization in the inversion process [e.g., *Yagi et al.*, 2003]. Bottoms of the seismogenic zones were defined independently of these large earthquakes by the references cited.
[d]*Hsu et al.* [2006].
[e]*Peterson and Seno* [1984] and *Scholz and Campos* [1995].
[f]*Pacheco et al.* [1993].
[g]*Briggs et al.* [2006].
[h]*Simoes et al.* [2004].
[i]*von Huene and Scholl* [1991].
[j]*Plank and Langmuir* [1998].
[k]*Subarya et al.* [2006] and *Hashimoto et al.* [2006]. These values are less than the report of a postseismic displacement from *Vigny et al.* [2005], since the large postseismic displacement at PHKT (1.25 times coseismic) does not appear in other analyses (R. Bürgmann, personal communication, 2006).
[l]*Ammon et al.* [2005].
[m]*Miyazaki et al.* [2004].
[n]*Tichelaar and Ruff* [1993].
[o]*Ruegg et al.* [2001].
[p]*Melbourne et al.* [2002].
[q]*Pritchard* [2003].
[r]*Zhang and Schwartz* [1992] and *Tavera and Buforn* [2001].
[s]*Schweller et al.* [1981].
[t]*Bürgmann et al.* [2001] and *Gordeev et al.* [2001].
[u]*Zobin and Levina* [2001].
[v]*Hirose et al.* [1999], *Yagi et al.* [2001], *Ozawa et al.* [2001], and *Miyazaki et al.* [2003].
[w]This region is transitional between the highly coupled Nankai Trough and weakly coupled Ryuku arc [e.g., *Miyazaki et al.*, 2003].
[x]*Oleskevich et al.* [1999].
[y]*Hutton et al.* [2002].
[z]*Manea et al.* [2003].
[aa]This study.
[bb]*Chlieh et al.* [2004].
[cc]*Heki et al.* [1997], *Heki and Tamura* [1997], *Nishimura et al.* [2000], and *Yagi et al.* [2003].
[dd]*Kawasaki et al.* [2001].
[ee]*Kawasaki et al.* [1995].
[ff]*Yamanaka and Kikuchi* [2004].

underestimated by the campaign GPS data because the deformation may change in sign during this long interval. Campaign GPS measurements do not begin until several months after the earthquake (Figure 3), but any rapid deformation could be detected by the one continuous GPS station in the city of Antofagasta [*Melbourne et al.*, 2002], and a SAR scene from track 96 acquired 9.5 hours after the earthquake. There is no obvious deformation during the first month after the M_w 8.1 earthquake at the continuous GPS station in Antofagasta [*Melbourne et al.*, 2002], but our joint study of all data sets (including the null result from the continuous site) indicates that this station was not well positioned to detect deformation during this time interval.

[11] We give greater weight to the GPS observations because they are not affected by spatial variations in the orbital parameters like the InSAR data. The weighting factor was empirically chosen to be a factor of 100, which is to an order of magnitude the ratio of the number of InSAR/GPS data points used in the inversion (there are roughly 100 total GPS data points and 20,000 subsampled InSAR points). However, the GPS displacements might be systematically in error if the reference frame for stable South America is incorrect. For example, the GPS measurements of *Chlieh et al.* [2004] and *Khazaradze and Klotz* [2003] define stable South America differently. Although we place both GPS measurements in the same reference frame [e.g., *Angermann et al.*, 1999], because this reference

frame might be incorrect, in our final inversion we solve for additional reference frame correction where we solve for a translation and a linear function of latitude and longitude for each horizontal GPS component. We bound this total shift to be less than 5 mm/yr. We have also run tests where we do not allow for this reference frame correction, and while the model results are not identical, they do not affect our interpretation.

3. Modeling Strategy

3.1. Mechanism of Deformation

[12] Measurements of deformation immediately following several subduction zone earthquakes reveal that a large amount of slip can occur aseismically during a few weeks to months (see references in Table 2). This postseismic deformation occurs over a much shorter period than would be expected for viscoelastic relaxation of the overriding plate (years to decades). In the specific case of the 1995 Jalisco earthquake, viscoelastic relaxation models provide a poor fit to the observed GPS displacements [*Azúa et al.*, 2002].

[13] Besides bulk viscoelastic processes, poroelastic processes have also been inferred as a primary source of postseismic deformation for shallow strike-slip earthquakes [e.g., *Peltzer et al.*, 1996; *Jónsson et al.*, 2003]. Subsurface fluid flow following the 1995 earthquake is suggested based on independent evidence [*Husen and Kissling*, 2001; *Koerner et al.*, 2004] and may also contribute to postseismic deformation. A simple calculation for northern Chile (using plausible values for the drained and undrained Poisson's ratio [*Rice and Cleary*, 1976]) indicates that the direction of deformation is opposite that observed and the amplitude is probably an order of magnitude too small [*Pritchard*, 2003].

[14] Because of the rapid timescale of deformation, and the inability of our poroelastic model to explain all of the deformation, we adopt an afterslip model where the postseismic deformation is explained by slip on the megathrust interface or across a relatively thin fault zone [e.g., *Heki et al.*, 1997].

3.2. Model Parameterization

[15] We adopt the same fault planes for the afterslip model that we used previously in inversions for coseismic slip [*Pritchard et al.*, 2002, 2006] with a strike of 5° east of north (same as the trench) and a dip that varies with depth from about 18–24° defined by aftershock locations from the 1995 earthquake and well constrained by a local network of onshore and offshore seismometers [*Husen et al.*, 1999]. We assume an elastic, Poissonian, homogeneous half-space, but also tested a one-dimensional layered crustal model also constrained with local data [*Husen et al.*, 1999]. Because the layered model results do not significantly differ from the homogeneous results (as discussed below) the figures only show results from the homogeneous models. In addition, we have tested different configurations of subfaults (changing subfault size including larger subfaults near the trench, see below). We only show results here from models with a uniform subfault size of 20 km by 20 km. Slip is not allowed to have a left-lateral component (consistent with plate convergence).

3.3. Temporal Resolution

[16] We divide the set of overlapping GPS and InSAR observations following the 1995 earthquake (Figure 3 and Table 1) into several temporal subdomains spanning 1995–2000. The deformation observed in each interferogram or set of GPS displacements is a linear combination of the deformation in one or more subdomains. Previous studies that have used temporal subdomains have inverted the observations for the deformation in each subdomain [*Lundgren et al.*, 2001; *Schmidt and Bürgmann*, 2003]. Our methodology inverts the observations for slip on the fault plane, which can be used to calculate the deformation in each temporal subdomain. Our inversion minimizes the roughness of slip in space and time (calculated using a discretized Laplacian operator) where the relative weighting of these a priori constraints have been chosen empirically, not formally as in, for example, the Network Inversion Filter [e.g., *Segall and Matthews*, 1997] because of our more temporally limited data sets.

[17] The start and end times for our temporal subdomains do not conform exactly to the time span of GPS campaigns or interferograms, but we chose temporal subdomains that are near such points (Figure 3). For example, a GPS campaign ends in October–November 1996, while we have several interferograms that begin/end in December 1996, so we specify the beginning/ending of one temporal subdomain with all of these observations. To account for the small amount of deformation that might occur between the start/end of a subdomain and the start/end of a set of observations, we scale up or down the magnitude of deformation by the relative time span of the data to the duration of the temporal subdomain. The mean correction necessary for the temporal subdomains was about 110% of a given subdomain. We only use geodetic data that do not span the 1995 earthquake, to avoid inferring afterslip from errors in modeling coseismic slip.

3.4. Removing Interseismic Deformation

[18] We pursue two strategies for separating afterslip from interseismic strain accumulation. In one set of models, we first remove an assumed back-slip model [*Savage*, 1983] of interseismic deformation from all of the data, and then solve for slip on the fault interface (where the dip-slip component is forced to be reverse, and the strike-slip component is forced to be right lateral, in accordance with plate convergence). We consider two different interseismic models that have been proposed to explain the local GPS data. In the first model, the fault interface is completely locked to 50 km with no transition zone. A 50-km-deep locked zone was favored by previous studies to the north and south of our study area [*Bevis et al.*, 2001; *Brooks et al.*, 2003]. Using different data than these studies, *Khazaradze and Klotz* [2003] chose a shallower locking depth south of 25°S, but our preliminary analysis of all available GPS data does not support a large change in locking depth between 21°–27°S. The second interseismic model has the fault interface locked to 35 km, with a transition zone to 59 km depth, consistent with analysis of GPS and InSAR data from our study area northward [*Chlieh et al.*, 2004].

[19] As an alternative to explicitly removing an interseismic model, we can model the data allowing for normal slip on the plate interface. Instead of removing an a priori model

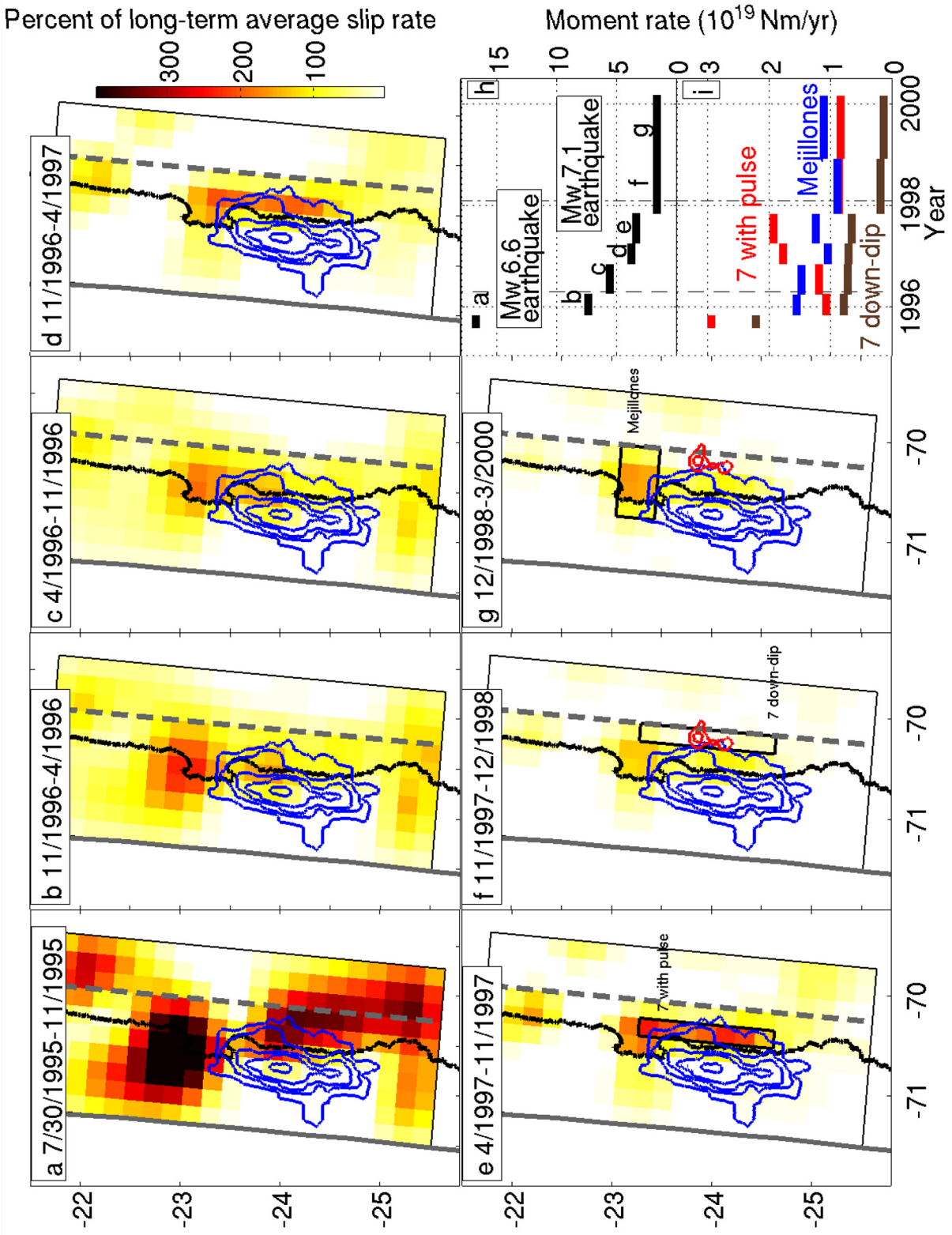
Percent of long-term average slip rate
300
200
100
Moment rate (10^{19} Nm/yr)
a 7/30/1995-11/1995
b 11/1996-4/1996
c 4/1996-11/1996
d 11/1996-4/1997
e 4/1997-11/1997
f 11/1997-12/1998
g 12/1998-3/2000
h
i
Mw6.6 earthquake
Mw7.1 earthquake
7 with pulse
Mejillones
7 down-dip
Year
-22
-23
-24
-25
-70
-71
1996
1998
2000

Figure 6

as described in the last paragraph, we directly solve for the best fitting distribution of slip, where we do not constrain the direction of slip; that is, both normal and reverse slip are allowed at all depths within the model. This model includes spatial and temporal smoothing, but otherwise no constraint on rake or slip direction. Although any inferred normal slip is not physical, this mode of slip can be used to account for interseismic locking, and is widely used to simulate interseismic deformation [*Savage*, 1983]. The details of our final models depend on how the interseismic deformation is removed, but the general conclusions as discussed below are similar in all models, thus we only show results from one suite of interseismic models using the 50-km-deep locked zone of *Bevis et al.* [2001].

4. Results

[20] The postseismic spatiotemporal evolution of slip and the inferred seismic moment rate as a function of time are shown in Figure 6. Our model indicates a decay time of slip between 1995 and 2000 of about 1 year (Figure 6h), consistent with theoretical models of afterslip [*Marone*, 1998]. For this model, we have removed an interseismic model of deformation (fault interface locked to 50 km), and use uniform subfault size in a homogeneous half-space. Predictions of the model for surface deformation are compared with GPS and InSAR data in Figures 4 and 5.

[21] Interseismic models that allow for normal and reverse slip provide better fits to the data (as expected, because of the larger parameter space), but the overall moment and gross properties of the slip distribution are similar to the results shown (including the slip pulse discussed below).

[22] Inversions for slip that only include GPS data predict sizable vertical deformation in gaps in the data coverage that is not consistent with the spatially continuous InSAR results. For the first subdomain, the GPS data favor having afterslip near the Mejillones Peninsula, while the InSAR data places it further south. The difference in the location of afterslip from the two data sets might just be an artifact due to the inherent trade-offs in the InSAR data between the location of slip and the orbital ramps. However, we cannot rule out the possibility that the afterslip occurs in the two locations at different times (the InSAR data covers the first months postseismic, while the campaign GPS data starts later).

4.1. Spatial Location of Slip

[23] The cumulative seismic slip by earthquakes during the past 18 years and aseismic slip over a 5-year period in northern Chile shows a complex spatiotemporal evolution [*Pritchard et al.*, 2006] (Figure 7). Despite the inherent smoothing associated with our inversions, there is little overlap between the different seismic and aseismic slip events, although other seismic and/or aseismic slip events are required (either in the past or future) so that the same total slip is accommodated over the fault. For example, while parts of the fault slipped 6 m in the 1995 main shock, other portions have slipped only a few tens of cm. We note that our cumulative slip map could be incomplete, because we can only detect slip that causes a maximum surface deformation signal of $\sim$1 cm.

[24] Slip in the 1995 main shock initiated near the Mejillones Peninsula but ruptured away from it toward the south with little coseismic slip below the peninsula [e.g., *Ruegg et al.*, 1996; *Ihmlé and Ruegg*, 1997; *Delouis et al.*, 1997; *Pritchard et al.*, 2006]. However, we find long term aseismic slip beneath the peninsula, although the cumulative slip over 5 years of observation is much less than in the region that ruptured in the 1995 main shock. In fact, the average rate of fault slip ($\sim$10 cm/yr) beneath the peninsula between 1995 and 2000 is nearly twice the plate convergence rate ($\sim$6 cm/yr). If sustained over a significant portion of the seismic cycle, this rate of slip would imply that large earthquakes are not likely to rupture beneath the peninsula. At face value, in order to not exceed the long-term slip budget, late in the seismic cycle this region would need to slip at a rate lower than the plate convergence rate and thereby would appear more coupled than the long-term average for this area. Another possibility is that aseismic slip may be episodic and either trigger or be triggered by seismic events.

[25] No large earthquakes have ruptured directly beneath the peninsula, and the $M_w > 6$ earthquakes shown in Figure 7 seem to occur near the edges of the regions that slipped postseismically. This behavior is consistent with the notion that the earthquakes are driven by the stressing rate associated with afterslip [*Perfettini and Avouac*, 2005]. There is some overlap between the afterslip and coseismic slip (from the 1995 main shock and aftershocks), but the maximum afterslip seems to occur near the Mejillones Peninsula in a region with no significant seismic activity ($M_w > 6.5$). The bulk of afterslip is deeper than the 1995 rupture zone, as found by *Chlieh et al.* [2004]. The Coulomb stress change

Figure 6. (a–g) Fault slip during each of the temporal subdomains normalized to represent the fraction of the plate convergence rate [*Angermann et al.*, 1999]. The coastline is shown as the black line, the trench is shown as a gray line, and the assumed depth to full interseismic locking (50 km) is the dotted gray line [*Bevis et al.*, 2001]. Blue contours show the 1995 coseismic slip [*Pritchard et al.*, 2006] at 1-m contour interval, while red contours indicate slip from the 1998 earthquake [*Pritchard et al.*, 2006] with contours at 0.5 m and 1.5 m (red contours are only shown after the earthquake occurs). (h) Seismic moment rate in each subdomain for all subfaults, calculated using vector summation of the slip vectors. Total moment is about 2×10^{20} N m (M_w 7.5). (i) Seismic moment rate in each subdomain for three subsets of subfaults. The red lines labeled "7 with pulse" show the time evolution of the pulse of slip on seven patches between the 1995 and 1998 ruptures (shown in Figure 6e). The blue lines labeled "Mejillones" show 8 subfaults (shown in Figure 6g) beneath the Mejillones Peninsula showing a long decay time. The brown lines labeled "7 downdip" are the seven subfaults immediately downdip of the 7 with the pulse of deformation (shown in Figure 6f). The region corresponding to the 7 downdip returns to interseismic deformation after 1998 despite being next to the subfaults with a pulse and the presence of spatial smoothing in the inversion.

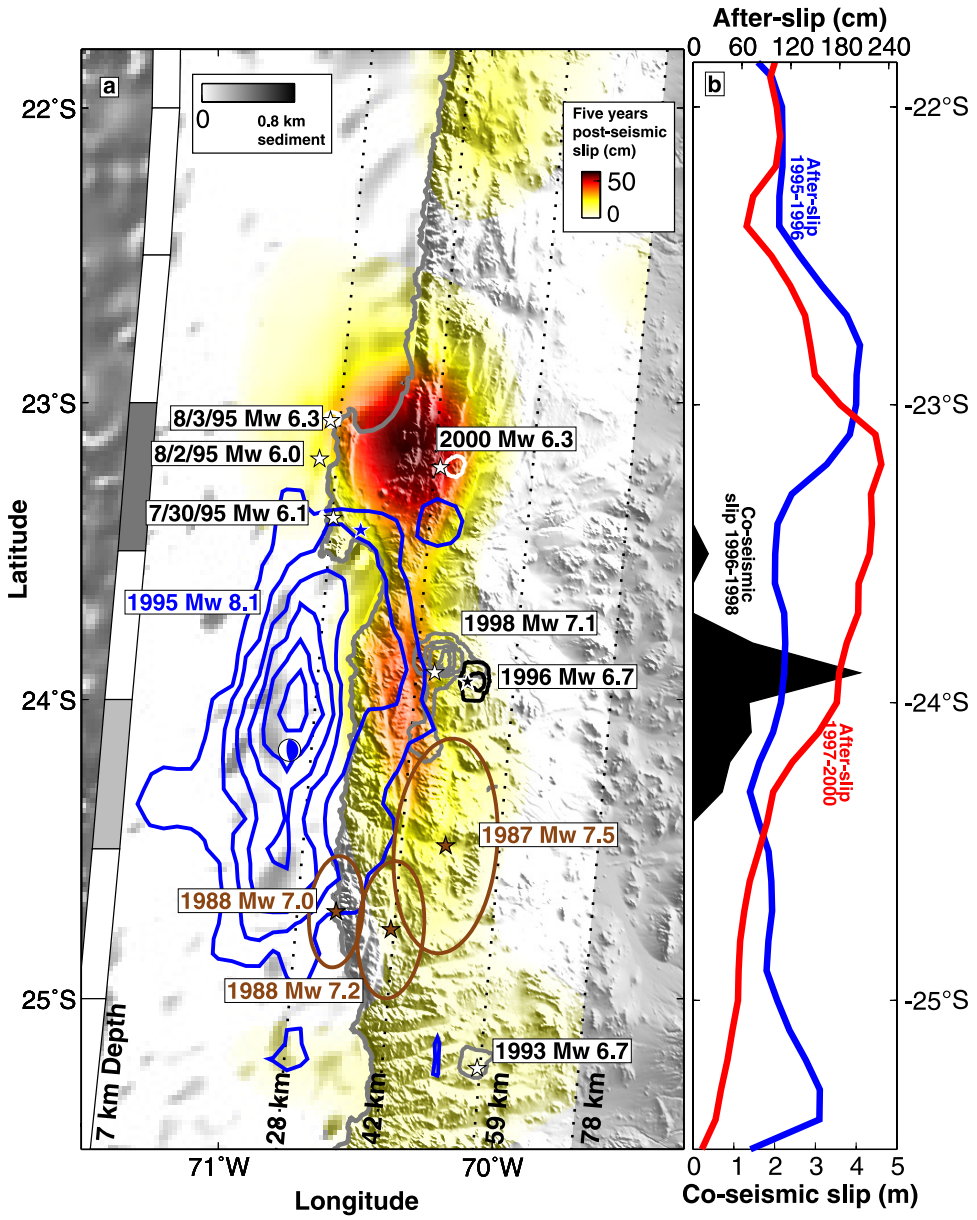

Figure 7. (a) Magnitude of slip on the fault interface (color) in the northern Chile subduction zone from aseismic slip and earthquakes with $M_w > 6.0$ since 1987 over shaded topography. Contours of coseismic slip [*Pritchard et al.*, 2006] from the 1995 main shock (1-m interval) and aftershocks ($M_w > 6$) between 1995 and 2000 (0.5 m interval). The brown ellipses with no contours are from earthquakes in the 1980s and are scaled assuming a constant stress drop for all events of 1.4 MPa [*Pritchard et al.*, 2006] and a length to width aspect ratio of 2. Depths on the fault interface are for the 1995 earthquake (black dotted lines labeled at bottom), but because some of the other events have slightly different dips, they might be a few kilometers off the reference depths. The trench location is shown as a series of boxes showing the amount of sediment in the trench (Figure 2), the coastline is shown as a thick gray line, and the depth to full interseismic locking (50 km) is the dashed gray line [*Bevis et al.*, 2001]. (b) Profiles of afterslip as a function of latitude (colored lines, scale at top) and coseismic slip between 1996 and 1998 (black region, scale at bottom). At each latitude, we sum the values at all longitudes from Figure 7a. Two time periods of afterslip are shown: from 1995 to 1996 (temporal subdomains in Figures 6a–6c, blue line) and from 1997 to 2000 (temporal subdomains in Figures 6d–6g, red line).

caused by the M_w 8.1 earthquake is highest to the northeast of the rupture, including the Mejillones Peninsula, possibly explaining the location of most aftershocks and the afterslip [*Lin and Stein*, 2004], although this does not explain the extreme localization beneath the Mejillones Peninsula itself. Alternatively, the fault frictional properties favor aseismic slip beneath the Mejillones Peninsula, and this possibility is further explored in the discussion.

4.2. Pulse of Slip

[26] There are a few regions where the evolution of afterslip does not follow a simple monotonic trend. For example, seven subfaults downdip of the 1995 earthquake and updip of the 1998 M_w 7.1 earthquake (Figure 6) show a decline in slip between 1995 and 1996, but then an episode of faster slip rate in 1997 that ends at about the time of the M_w 7.1 earthquake. The pulse may have been triggered by previous postseismic deformation or the 1996 M_w 6.7 aftershock (Figure 7). More importantly, the pulse is immediately updip of the 1998 M_w 7.1 earthquake and may have triggered this event. The aseismic pulse is located within a depth range of 35–40 km, which, in this general region, is also a depth interval where earthquakes nucleate. The depth of this aseismic pulse is similar to that associated with the observed aseismic transients in Japan (15–40 km) [*Ozawa et al.*, 2004], Mexico (22–47 km) [*Yoshioka et al.*, 2004] and Cascadia (30–40 km) [*Dragert et al.*, 2001].

[27] The total associated moment over the 1995–2000 time period and over the entire modeled fault plane is $2–4 \times 10^{20}$ Nm (equivalent to $M_w \sim 7.6$), which is only about 10–20% of the coseismic moment (assuming a rigidity of 50 GPa). The range in moment comes from the variety of models that we tested, and is similar to a previous result using an independent method and a subset of the InSAR and GPS data [*Chlieh et al.*, 2004].

[28] The overall moment of the aseismic pulse (5×10^{19} N m, M_w 7.1) is several times larger than the 1996 aftershock (1.5×10^{19} N m, M_w 6.7) [*Pritchard*, 2003; *Pritchard et al.*, 2006] and is slightly smaller than the 1998 aftershock (6.1×10^{19} N m, M_w 7.1) [*Pritchard*, 2003; *Pritchard et al.*, 2006], although the pulse appears to rupture a larger fault area (implying a lower stress drop).

[29] The seven subfaults where we observed the slip pulse in 1997 have anomalous behavior in all of the models we have tested that use InSAR data with or without GPS data. However, whether the region associated with these seven subpatches actually had a pulse (a decline and then an increase in slip) or just a much slower decline than the other subfaults depends on the data sets used and the constraints applied. We do not think that the pulse is afterslip from the 1996 earthquake, because there is a clearly resolved six month delay between the start of the pulse and the earthquake (Figure 6i). The pulse may have been triggered by previous postseismic deformation or the 1996 aftershock. In turn, the pulse is immediately updip of the 1998 earthquake and may have helped trigger this event. We were concerned that the slip pulse could be unmodeled deformation from the 1998 earthquake, but the pulse still exists even when we exclude interferograms that include this earthquake. Further data from the continuous GPS station in Antofagasta could potentially be used to test the reality of this pulse (although the predicted signal is only a few cm and mostly vertical), but these data are not presently available to the authors.

5. Discussion

[30] For the large and great subduction zone earthquakes of the last 15 years, we compile the ratio of cumulative afterslip to the size of the main shock and other information in Table 2. In general, afterslip is likely underestimated in Table 2 because some deformation may not be detected if the spatial extent of measurements is limited (e.g., few stations near the trench). Table 2 only includes data from the first year or less after the earthquake and thus misses any long-term viscoelastic deformation. The amount of rapid afterslip following the 1995 earthquake is low compared to other recent subduction zone earthquakes, including the nearby M_w 8.4 earthquake in southern Peru in 2001 (Figure 2). Table 2 shows that these global variations in the amount of afterslip are not predicted on the basis of the seismic coupling coefficient (χ, the ratio of the observed moment in earthquakes to that expected from plate convergence). In general, χ is not well constrained, because of the incompleteness of the seismic record and the absence of local networks [e.g., *McCaffrey*, 1997].

5.1. Along-Strike Frictional Variations

[31] There are at least three possible explanations for local and global variations in the magnitude of afterslip [*Marone*, 1998]: (1) different initial conditions; (2) different coseismic excitation of the frictionally stable materials that undergo afterslip; and (3) different properties of the frictionally stable materials, making them more or less susceptible to afterslip. It has proven difficult to determine which of these explanations is most important [*Marone*, 1998; *Melbourne et al.*, 2002], in part because the spatial variations in the initial stress conditions are not known. Since subduction zone earthquakes spanning more than 3 orders of magnitude in seismic moment all have considerable afterslip, it appears that other factors must exert considerable control on variations in afterslip [*Melbourne et al.*, 2002]. Indeed, several observations suggest that fault frictional properties vary spatially both within a single subduction zone and between subduction zones [*Song and Simons*, 2003; *Wells et al.*, 2003; *Miyazaki et al.*, 2004; *Hsu et al.*, 2006].

[32] For example, afterslip following the 1995 earthquake is not limited to immediately downdip of the coseismic rupture (Figure 7), as would be expected if there is only a simple depth progression of frictional properties on the fault interface. In other subduction zones, afterslip has been inferred to occur mostly downdip of the coseismic rupture of a main shock [*Thatcher and Rundle*, 1984; *Hutton et al.*, 2002; *Yagi et al.*, 2003]. In northern Chile, both seismic and aseismic slip occurred in nearby areas within the same depth range, indicating that there is not a uniform depth at which there is a sharp transition between materials that slip in earthquakes or in aseismic events. The maximum time-integrated amount of afterslip occurred near the Mejillones Peninsula (up to 100 km from the maximum coseismic slip, and not downdip of the M_w 8.1 event). Furthermore, the longer-lived afterslip and the suggested lack of coupling below the peninsula (previously unsuspected) may be consistent with different material properties on the underlying fault plane [*Song and Simons*, 2003] (Figure 6h). These observations along with a handful of studies from Japan [*Miyazaki et al.*, 2003, 2004] and Sumatra [*Subarya et al.*, 2006; *Hsu et al.*, 2006], suggest that along-strike variations in the frictional properties may play a critical role in controlling variations in afterslip. Furthermore, we document a significant earthquake ($M_w \sim 7$) occurring downdip of both the main shock and the majority of the afterslip, suggesting that frictional behavior does not vary monotonically with depth, or may vary with time.

[33] The 2.5-year delay between the largest aftershock (M_w 7.1 in 1998) and the 1995 main shock is statistically unusual [*Reasenberg and Jones*, 1989], suggesting that it is not a conventional aftershock, but rather triggered by the adjacent transient slip pulse. More generally, a long time delay between aftershocks and the main shock may suggest the influence of aseismic slip in other subduction zones. These are the first observations with sufficient resolution in both time and space to infer triggering of a large ($M_w > 7$) earthquake by an aseismic slip event, although, for example, continued afterslip following the M_w 7.5, 1999, İzmit, Turkey, strike-slip earthquake may have contributed to triggering of the M_w 7.2, 1999, Düzce, Turkey, earthquake [*Bürgmann et al.*, 2002].

5.2. Correlation Between Sediments and Afterslip

[34] On a larger scale, properties of the subduction zone (e.g., plate age and rate of convergence) are similar in southern Peru and northern Chile [*Müller et al.*, 1997; *Angermann et al.*, 1999]. Thus a simple interpretation in terms of depth variations of temperature or broadscale variations in normal tractions on the fault interface is not sufficient to explain the variations in afore mentioned afterslip. In contrast, estimates of sediment thickness in the Peru-Chile trench, indicate an along-strike variation in the amount of sediment subducted (Figure 2) [*Schweller et al.*, 1981]. Thus we emphasize here the potential importance of sediments.

[35] A global compilation of afterslip in subduction zones suggests that regions of significant afterslip have several hundred meters of sediment uniformly distributed in the trench, while regions with less afterslip have virtually no sediment (Table 2). Such variations in sediment may also control local variations in afterslip, suggested by the presence of afterslip beneath the Mejillones Peninsula and a sediment filled basins in the trench immediately west of the peninsula [*Schweller et al.*, 1981].

[36] We list the estimates of the thickness of sediment being subduction in each region in Table 2. These values should be used with caution because sediment thickness vary greatly along strike, and many places only have a single measurement [e.g., *Plank and Langmuir*, 1998]. Where available, we have used values for sediment thickness directly from the area of coseismic rupture [*Manea et al.*, 2003; *Schweller et al.*, 1981; *Curry*, 1994]. A further complication is that the thickness of sediment in the trench may be more or less than the thickness of sediment being subducted. For example, in northeast Japan, the thickness of sediment in the trench is 200–400 m, but a sediment channel of more than 1 km may exist at a depth of 12 km because of basal erosion [*von Huene et al.*, 1994]. Also, the morphology of the subducting slab can affect the distribution of the sediment, and its effect on seismogenesis or the generation of aseismic slip. Again in northeast Japan, the variable along-strike presence of horst-and-graben structure that can trap sediments has been linked to along-strike variations in seismogenesis [*Tanioka et al.*, 1997]. Finally, the composition of the sediment is not globally uniform [*Rea and Ruff*, 1996; *Plank and Langmuir*, 1998], and certain sediments may be more or less likely to encourage afterslip.

[37] The presence of subducted sediments does not cause completely aseismic fault slip: some of the largest earthquakes have ruptured areas with significant sediment subduction [*Ruff*, 1989]. However, sediments and the fluids they contain may change the thermal and mechanical properties of the fault to promote aseismic afterslip. For example, sediments may "smooth out" fault irregularities encouraging aseismic slip over broader areas, in a manner similar to the proposed role of sediments in encouraging great earthquakes [*Ruff*, 1989]. In addition, sediments appear to increase the maximum depth of seismicity [*Zhang and Schwartz*, 1992], and this might explain why the 2001 earthquake in southern Peru (where the sediments are thicker) ruptured to a deeper depth than the 1995 earthquake in northern Chile [*Pritchard et al.*, 2002; *Pritchard*, 2003].

[38] If the amount of sediments do control the afterslip properties, we would predict there to be little afterslip (perhaps less than 20% of the coseismic moment) following the earthquake that reruptures the location of the 1877 earthquake in northern Chile and the remainder of the 1868 rupture area in southern Peru (Figure 2). In addition, the maximum depth of fault rupture in this event should be more similar to the 1995 earthquake than the 2001 earthquake. More generally, we predict regions with little trench filling sediments [*Ruff*, 1989] will experience small amounts of afterslip relative to the size of the local earthquakes, while regions with thick sediments [*Ruff*, 1989], should experience relatively larger amounts of afterslip.

[39] As the spatial and temporal density of geodetic data increases, we may find more evidence for the complex distribution of seismogenic behavior on the plate interface in subduction zones that is not simply correlated with temperatures and large-scale plate tectonic forces. This complexity in slip behavior has several implications for seismic hazard assessment, including the potential maximum size of subduction zone earthquakes within a region, and whether a particular segment is likely to have large earthquakes at all.

[40] **Acknowledgments.** ERS SAR imagery for this study was acquired as a category 1 research project from the European Space Agency. We thank R. Bürgmann, T. Baba, and Associate Editor S. Cohen for critical reviews, as well as M. Chlieh, H. Kanamori, J. Klotz, T. Heaton, and M. Gurnis for discussions. GMT was used to create several figures [*Wessel and Smith*, 1998]. M.E.P. was partly supported by a Hess postdoctoral fellowship at Princeton University. This is Caltech Tectonics Observatory contribution 41 and Caltech Seismological Laboratory contribution 9151.

References

Ammon, C. J., et al. (2005), Rupture process of the 2004 Sumatra-Andaman earthquake, *Science*, *308*, 1133–1139.

Angermann, D., J. Klotz, and C. Reigber (1999), Space-geodetic estimation of the Nazca–South America Euler vector, *Earth Planet. Sci. Lett.*, *171*, 329–334.

Azúa, B. M., C. DeMets, and T. Masterlark (2002), Strong interseismic coupling, fault afterslip, and viscoelastic flow before and after the Oct. 9, 1995 Colima-Jalisco earthquake: Continuous GPS measurements from Colima, Mexico, *Geophys. Res. Lett.*, *29*(8), 1281, doi:10.1029/2002GL014702.

Beauducel, B., P. Briole, and J.-L. Foger (2000), Volcano-wide fringes in ERS synthetic aperture radar interferograms of Etna (1992–1998): Deformation or tropospheric effect?, *J. Geophys. Res.*, *105*, 16,391–16,402.

Beck, S. L., S. Barrientos, E. Kausel, and M. Reyes (1998), Source characteristics of historic earthquakes along the central Chile subduction zone, *J. S. Am. Earth Sci.*, *11*, 115–129.

Bevis, M., E. C. Kendrick, R. Smalley Jr., T. Herring, J. Godoy, and F. Galban (1999), Crustal motion north and south of the Arica deflection: Comparing recent geodetic results from the central Andes, *Geochem. Geophys. Geosyst.*, *1*(1), doi:10.1029/1999GC000011.

Bevis, M., E. Kendrick, R. Smalley Jr., B. Brooks, R. Allmendinger, and B. Isacks (2001), On the strength of interplate coupling and the rate of back arc convergence in the central Andes: An analysis of the interseismic

velocity field, *Geochem. Geophys. Geosyst.*, *2*(11), doi:10.1029/2001GC000198.

Briggs, R. W., et al. (2006), Deformation and slip along the Sunda megathrust in the great 2005 Nias-Simeulue earthquake, *Science*, *311*, 1897–1901.

Brooks, B. A., M. Bevis, R. Smalley Jr., E. Kendrick, R. Manceda, E. Laura, R. Maturana, and M. Araujo (2003), Crustal motion in the southern Andes (26°–36°S): Do the Andes behave like a microplate?, *Geochem. Geophys. Geosyst.*, *4*(10), 1085, doi:10.1029/2003GC000505.

Bürgmann, R., M. G. Kogan, V. E. Levin, C. H. Scholz, R. W. King, and G. M. Steblov (2001), Rapid aseismic moment release following the 5 December, 1997 Kronotsky, Kamchatka, earthquake, *Geophys. Res. Lett.*, *28*, 1331–1334.

Bürgmann, R., S. Ergintav, P. Segall, E. H. Hearn, S. McClusky, R. E. Reilinger, H. Woith, and J. Zschau (2002), Time-dependent distributed afterslip on and deep below the İzmit earthquake rupture, *Bull. Seismol. Soc. Am.*, *92*, 126–137.

Chlieh, M., J. B. de Chabalier, J. C. Ruegg, R. Armijo, R. Dmowska, J. Campos, and K. Feigl (2004), Crustal deformation and fault slip during the seismic cycle in the north Chile subduction zone, from GPS and InSAR observations, *Geophys. J. Int.*, *158*, 695–711.

Comte, D., and M. Pardo (1991), Reappraisal of great historical earthquakes in the northern Chile and southern Peru seismic gaps, *Nat. Hazards*, *4*, 23–44.

Curry, J. R. (1994), Sediment volume and mass beneath the Bay of Bengal, *Earth Planet. Sci. Lett.*, *125*, 371–383.

Delouis, B., et al. (1997), The M_W = 8.0 Antofagasta (northern Chile) earthquake of 30 July 1995: A precursor to the end of the large 1877 gap, *Bull. Seismol. Soc. Am.*, *87*, 427–445.

Dragert, H., K. Wang, and T. S. James (2001), A silent slip event on the deeper Cascadia interface, *Science*, *292*, 1525–1528.

Farr, T. G., and M. Kobrick (2000), Shuttle Radar Topography Mission produces a wealth of data, *Eos Trans. AGU*, *81*(48), 583, 585.

Gordeev, E. I., A. A. Gusev, V. E. Levin, V. F. Bakhtiarov, V. M. Pavlov, V. N. Chebrov, and M. Kasahara (2001), Preliminary analysis of deformation at the Eurasia-Pacific-North America plate junction from GPS data, *Geophys. J. Int.*, *147*, 189–198.

Hashimoto, M., N. Choosakul, M. Hashizume, S. Takemoto, H. Takiguchi, Y. Fukada, and K. Fujimori (2006), Crustal deformations associated with the great Sumatra-Andaman earthquake deduced from continuous GPS observation, *Earth Planets Space*, *58*, 127–139.

Hearn, E. H., R. Bürgmann, and R. E. Reilinger (2002), Dynamics of İzmit earthquake postseismic deformation and loading of the Düzce earthquake hypocenter, *Bull. Seismol. Soc. Am.*, *92*, 172–193.

Heki, K., and Y. Tamura (1997), Short-term afterslip in the 1994 Sanriku-Haruka-Oki earthquake, *Geophys. Res. Lett.*, *21*, 3285–3288.

Heki, K., S. Miyazaki, and H. Tsuji (1997), Silent fault slip following an interplate thrust earthquake at the Japan Trench, *Nature*, *386*, 595–598.

Hirose, H., K. Hirahara, F. Kimata, N. Fukii, and S. Miyazaki (1999), A slow thrust slip event following the two 1996 Hyugada earthquakes beneath the Bungo Channel, southwest Japan, *Geophys. Res. Lett.*, *26*, 3237–3240.

Hsu, Y.-J., M. Simons, J.-P. Avouac, J. Galetzka, K. Sieh, M. Chlieh, D. Natawidjaja, L. Prawirodirdjo, and Y. Bock (2006), Frictional afterslip following the M_W 8.7, 2005 Nias-Simeulue earthquake, Sumatra, *Science*, *312*, 1921–1926.

Husen, S., and E. Kissling (2001), Postseismic fluid flow after the large subduction earthquake of Antofagasta, Chile, *Geology*, *138*, 847–850.

Husen, S., E. Kissling, E. Flueh, and G. Asch (1999), Accurate hypocentre determination in the seismogenic zone of the subducting Nazca Plate in northern Chile using a combined on-/offshore network, *Geophys. J. Int.*, *138*, 687–701.

Hutton, W., C. DeMets, O. SÁnchez, G. SuÁrez, and J. Stock (2002), Slip kinematics and dynamics during and after the 9 October 1995 M_W 8.0 Colima-Jalisco earthquake, Mexico, from GPS geodetic constraints, *Geophys. J. Int.*, *146*, 637–658.

Ihmlé, P. F., and J.-C. Ruegg (1997), Source tomography by simulated annealing using broad-band surface waves and geodetic data: Application to the M_W = 8.1 Chile 1995 event, *Geophys. J. Int.*, *131*, 146–158.

Jónsson, S., P. Segall, R. Pedersen, and G. BjÖrnsson (2003), Post-earthquake ground movements correlated to pore-pressure transients, *Nature*, *424*, 179–183.

Kanamori, H. (1986), Rupture process of subduction-zone earthquakes, *Annu. Rev. Earth Planet. Sci.*, *14*, 293–322.

Kawasaki, I., Y. Asai, Y. Tamura, T. Sagiya, N. Mikami, Y. Okada, M. Sakata, and M. Kasahara (1995), The 1992 Sanriku-Oki, Japan, ultra-slow earthquake, *J. Phys. Earth*, *43*, 105–116.

Kawasaki, I., Y. Asai, and Y. Tamura (2001), Space-time distribution of interplate moment release including slow earthquakes and the seismogeodetic coupling in the Sanriku-Oki region along the Japan trench, *Tectonophysics*, *330*, 267–283.

Kendrick, E. C., M. Bevis, J. R. F. Smalley, O. Cifuentes, and F. Galban (1999), Current rates of convergence across the central Andes: Estimates from continuous GPS observations, *Geophys. Res. Lett.*, *26*, 541–544.

Kendrick, E., M. Bevis, R. Smalley Jr., and B. Brooks (2001), An integrated crustal velocity field for the central Andes, *Geochem. Geophys. Geosyst.*, *2*(11), doi:10.1029/2001GC000191.

Khazaradze, G., and J. Klotz (2003), Short and long-term effects of GPS measured crustal deformation rates along the south central Andes, *J. Geophys. Res.*, *108*(B6), 2289, doi:10.1029/2002JB001879.

Klotz, J., et al. (1999), GPS-derived deformation of the central Andes including the 1995 Antofagasta M_W = 8.0 earthquake, *Pure Appl. Geophys.*, *154*, 709–730.

Klotz, J., G. Khazaradze, D. Angermann, C. Reigber, R. Perdomo, and O. Cifuentes (2001), Earthquake cycle dominates contemporary crustal deformation in central and southern Andes, *Earth Planet. Sci. Lett.*, *193*, 437–446.

Koerner, A., E. Kissling, and S. A. Miller (2004), A model of deep crustal fluid flow following the M_W = 8.0 Antofagasta, Chile, earthquake, *J. Geophys. Res.*, *109*, B06307, doi:10.1029/2003JB002816.

Lin, J., and R. S. Stein (2004), Stress triggering in thrust and subduction earthquakes and stress interaction between the southern San Andreas and nearby thrust and strike-slip faults, *J. Geophys. Res.*, *109*, B02303, doi:10.1029/2003JB002607.

Liu, Y., and J. R. Rice (2005), Aseismic slip transients emerge spontaneously in three-dimensional rate and state modeling of subduction earthquake sequences, *J. Geophys. Res.*, *110*, B08307, doi:10.1029/2004JB003424.

Lundgren, P., S. Usai, E. Sansosti, R. Lanari, M. Tesauro, G. Fornaro, and P. Berardino (2001), Modeling surface deformation with synthetic aperture radar interferometry at Campi Flegrei caldera, *J. Geophys. Res.*, *106*, 19,355–19,367.

Manea, M., V. C. Manea, and V. Kostoglodov (2003), Sediment fill in the Middle America Trench inferred from gravity anomalies, *Geofis. Int.*, *42*, 603–612.

Marone, C. (1998), Laboratory-derived friction laws and their application to seismic faulting, *Annu. Rev. Earth Planet. Sci.*, *26*, 643–696.

McCaffrey, R. (1997), Statistical significance of the seismic coupling coefficient, *Bull. Seismol. Soc. Am.*, *87*, 1069–1073.

Melbourne, T., F. Webb, J. Stock, and C. Reigber (2002), Rapid postseismic transients in subduction zones from continuous GPS, *J. Geophys. Res.*, *107*(B10), 2241, doi:10.1029/2001JB000555.

Miyazaki, S., J. J. McGuire, and P. Segall (2003), A transient subduction zone slip episode in southwest Japan observed by the nationwide GPS array, *J. Geophys. Res.*, *108*(B2), 2087, doi:10.1029/2001JB000456.

Miyazaki, S., P. Segall, J. Fukuda, and T. Kato (2004), Space time distributions of afterslip following the 2003 Tokachi-oki earthquake: Implications for variations in fault zone frictional properties, *Geophys. Res. Lett.*, *31*, L06623, doi:10.1029/2003GL019410.

Monfret, T., L. Dorbath, J. P. Caminade, M. Pardo, D. Comte, and L. Ponce (1995), The July 30, Antofagasta earthquake: An 'hypocritical' seismic event (abstract), *Eos Trans. AGU*, *76*, 427.

Montési, L. (2004), Controls of shear zone rheology and tectonic loading on postseismic creep, *J. Geophys. Res.*, *109*, B10404, doi:10.1029/2003JB002925.

Müller, R. D., W. R. Roest, J. Y. Royer, L. M. Gahagan, and J. G. Sclater (1997), Digital isochrons of the world's ocean floor, *J. Geophys. Res.*, *102*, 3211–3214.

Nishimura, T., et al. (2000), Distribution of seismic coupling on the subducting plate boundary in northeastern Japan inferred from GPS observations, *Tectonophysics*, *323*, 217–238.

Norabuena, E., L. Leffler-Griffin, A. Mao, T. Dixon, S. Stein, I. S. Sacks, L. Ocola, and M. Ellis (1998), Space geodetic observations of Nazca-South America convergence across the central Andes, *Science*, *279*, 358–362.

Oleskevich, D. A., R. D. Hyndman, and K. Wang (1999), The updip and downdip limits to great subduction earthquakes: Thermal and structural models of Cascadia, south Alaska, SW Japan, and Chile, *J. Geophys. Res.*, *104*, 14,965–14,991.

Ozawa, S., M. Murakami, and T. Tada (2001), Time-dependent inversion study of the slow thrust event in the Nankai trough subduction zone, southwestern Japan, *J. Geophys. Res.*, *106*, 787–802.

Ozawa, S., Y. Hatanaka, M. Kaidzu, M. Murakami, T. Imakiire, and Y. Isigaki (2004), Aseismic slip and low-frequency earthquakes in the Bungo channel, southwestern Japan, *Geophys. Res. Lett.*, *31*, L07609, doi:10.1029/2003GL019381.

Pacheco, J. F., L. R. Sykes, and C. H. Scholz (1993), Nature of seismic coupling along simple plate boundaries of the subduction type, *J. Geophys. Res.*, *98*, 14,133–14,159.

Peltzer, G., P. Rosen, P. Rogez, and P. Hudnut (1996), Postseismic rebound in fault step-overs caused by pore fluid flow, *Science*, *273*, 1202–1204.

Perfettini, H., and J.-P. Avouac (2005), Stress transfer and strain rate variations during the seismic cycle, *J. Geophys. Res.*, *109*, B06402, doi:10.1029/2003JB002917.

Peterson, E. T., and T. Seno (1984), Factors affecting seismic moment release rates in subduction zones, *J. Geophys. Res.*, *89*, 10,233–10,248.

Plank, T., and C. H. Langmuir (1998), The chemical composition of subducting sediment and its consequences for the crust and mantle, *Chem. Geol.*, *145*, 325–394.

Pritchard, M. E. (2003), Recent crustal deformation in west-central South America, Ph.D. thesis, Calif. Inst. of Technol., Pasadena. (Available at http://etd.caltech.edu/etd/available/etd-06022003-105512/)

Pritchard, M. E., M. Simons, P. Rosen, S. Hensley, and F. Webb (2002), Coseismic slip from the 1995 July 30 M_W = 8.1 Antofagasta, Chile, earthquake as constrained by InSAR and GPS observations, *Geophys. J. Int.*, *150*, 362–376.

Pritchard, M. E., C. Ji, and M. Simons (2006), Distribution of slip from 11 $M_W > 6$ earthquakes in the northern Chile subduction zone, *J. Geophys. Res.*, doi:10.1029/2005JB004013, in press.

Rea, D. K., and L. J. Ruff (1996), Composition and mass flux of sediment entering the world's subduction zones: Implications for global sediment budgets, great earthquakes, and volcanism, *Earth Planet. Sci. Lett.*, *140*, 1–12.

Reasenberg, P. A., and L. M. Jones (1989), Earthquake hazard after a mainshock in California, *Science*, *243*, 1173–1176.

Rice, J. R., and M. P. Cleary (1976), Some basic stress diffusion solutions for fluid-saturated elastic porous media with compressible constituents, *Rev. Geophys.*, *14*, 227–241.

Rosen, P. A., S. Hensley, G. Peltzer, and M. Simons (1994), Updated Repeat Orbit Interferometry Package released, *Eos Trans. AGU*, *85*(5), 47.

Rosen, P. A., S. Hensley, H. A. Zebker, F. H. Webb, and E. J. Fielding (1996), Surface deformation and coherence measurements of Kilauea Volcano, Hawaii, from SIR-C radar interferometry, *J. Geophys. Res.*, *101*, 23,109–23,125.

Rosen, P. A., S. Hensley, I. R. Joughin, F. K. Li, S. N. Madsen, E. Rodríguez, and R. M. Goldstein (2000), Synthetic aperture radar interferometry, *Proc. IEEE*, *88*, 333–382.

Ruegg, J. C., et al. (1996), The M_W = 8.1 Antofagasta (north Chile) earthquake July 30, 1995: First results from teleseismic and geodetic data, *Geophys. Res. Lett.*, *23*, 917–920.

Ruegg, J. C., M. Olcay, and D. Lazo (2001), Co-, post- and pre(?)-seismic displacements associated with the M_W = 8.4 southern Peru earthquake of 23 June 2001 from continuous GPS measurements, *Seismol. Res. Lett.*, *72*, 673–678.

Ruegg, J. C., J. Campos, R. Madariaga, E. Kausel, J. B. de Chabalier, R. Armijo, D. Dimitrov, I. Georgiev, and S. Barrientos (2002), Interseismic strain accumulation in south central Chile from GPS measurements, 1996–1999, *Geophys. Res. Lett.*, *29*(11), 1517, doi:10.1029/2001GL013438.

Ruff, L. J. (1989), Do trench sediments affect great earthquake occurrence in subduction zones?, *Pure Appl. Geophys.*, *129*, 263–282.

Savage, J. C. (1983), A dislocation model of strain accumulation and release at a subduction zone, *J. Geophys. Res.*, *88*, 4984–4996.

Schmidt, D. A., and R. Bürgmann (2003), Time-dependent land uplift and subsidence in the Santa Clara valley, California, from a large interferometric synthetic aperture radar data set, *J. Geophys. Res.*, *108*(B9), 2416, doi:10.1029/2002JB002267.

Scholz, C. H., and J. Campos (1995), On the mechanism of seismic decoupling and back-arc spreading at subduction zones, *J. Geophys. Res.*, *100*, 22,103–22,115.

Schweller, W. J., L. D. Kulm, and R. A. Prince (1981), Tectonics, structure, and sedimentary framework of the Peru-Chile trench, in *Nazca Plate: Crustal Formation and Andean Convergence*, edited by L. D. Kulm, *Mem. Geol. Soc. Am.*, *154*, 323–349.

Segall, P., and M. Matthews (1997), Time dependent inversion of geodetic data, *J. Geophys. Res.*, *102*, 22,391–22,409.

Simons, M., Y. Fialko, and L. Rivera (2002), Coseismic deformation from the 1999 M_W 7.1 Hector Mine, California, earthquake as inferred from InSAR and GPS observations, *Bull. Seismol. Soc. Am.*, *92*, 1390–1402.

Simoes, M., J.-P. Avouac, R. Cattin, and P. Henry (2004), The Sumatra subduction zone: A case for a fault zone extending into the mantle, *J. Geophys. Res.*, *109*, B10402, doi:10.1029/2003JB002958.

Song, T.-R. A., and M. Simons (2003), Large trench-parallel gravity variations predict seismogenic behavior in subduction zones, *Science*, *301*, 630–633.

Subarya, C., M. Chlieh, L. Prawirodirdjo, J.-P. Avouac, Y. Bock, K. Sieh, A. J. Meltzner, D. H. Natawidjaja, and R. McCaffrey (2006), Plate-boundary deformation associated with the great Sumatra-Andaman earthquake, *Nature*, *440*, 46–51.

Tanioka, Y., L. Ruff, and K. Satake (1997), What controls the lateral variation of large earthquake occurrence along the Japan trench?, *Island Arc*, *6*, 261–266.

Tavera, H., and E. Buforn (2001), Source mechanism of earthquakes in Peru, *J. Seismology*, *5*, 519–539.

Thatcher, W., and J. B. Rundle (1984), A viscoelastic coupling model for the cyclic deformation due to periodically repeated earthquakes at subduction zones, *J. Geophys. Res.*, *89*, 7631–7640.

Tichelaar, B. W., and L. J. Ruff (1993), Depth of seismic coupling along subduction zones, *J. Geophys. Res.*, *98*, 2017–2037.

Vigny, C., et al. (2005), Insight into the 2004 Sumatra-Andaman earthquake from GPS measurements in Southeast Asia, *Nature*, *436*, 201–206.

von Huene, R., and D. W. Scholl (1991), Observations at convergent margins concerning sediment subduction, subduction erosion and the growth of continental crust, *Rev. Geophys.*, *29*, 279–316.

von Huene, R., D. Klaeschen, and B. Cropp (1994), Tectonic structure across the accretionary and erosional parts of the Japan trench margin, *J. Geophys. Res.*, *99*, 22,349–22,361.

Wells, R. W., R. J. Blakely, Y. Sugiyama, D. W. Scholl, and P. A. Dinterman (2003), Basin-centered asperities in great subduction zone earthquakes: A link between slip, subsidence, and subduction erosion?, *J. Geophys. Res.*, *108*(B10), 2507, doi:10.1029/2002JB002072.

Wessel, P., and W. H. F. Smith (1998), New, improved version of Generic Mapping Tools released, *Eos*, *79*, 579.

Xia, Y., G. W. Michel, C. Riegber, J. Klotz, and H. Kaufmann (1998), Seismic unloading and loading in northern central Chile as observed by differential synthetic aperture radar interferometry D-INSAR and GPS, *Int. J. Remote Sens.*, *24*, 4375–4391.

Yagi, Y., M. Kikuchi, and T. Sagiya (2001), Co-seismic slip, post-seismic slip, and aftershocks associated with two large earthquakes in 1996 in Hyuga-nada, Japan, *Earth Planets Space*, *53*, 793–803.

Yagi, Y., M. Kikuchi, and T. Nishimura (2003), Co-seismic slip, post-seismic slip, and largest aftershock associated with the 1994 Sanriku-harukaoki, Japan, earthquake, *Geophys. Res. Lett.*, *30*(22), 2177, doi:10.1029/2003GL018189.

Yamanaka, Y., and M. Kikuchi (2004), Asperity map along the subduction zone in northeastern Japan inferred from regional seismic data, *J. Geophys. Res.*, *109*, B07307, doi:10.1029/2003JB002683.

Yoshioka, S., T. Mikumo, V. Kostoglodov, K. M. Larson, A. R. Lowry, and S. K. Singh (2004), Interplate coupling and a recent aseismic slow slip event in the Guerrero seismic gap of the Mexican subduction zone as deduced from GPS data inversion using a Bayesian information criterion, *Phys. Earth Planet. Inter.*, *146*, 513–530.

Zebker, H. A., P. A. Rosen, R. M. Goldstein, A. Gabriel, and C. L. Werner (1994), On the derivation of coseismic displacement–fields using differential radar interferometry: The Landers earthquake, *J. Geophys. Res.*, *99*, 19,617–19,634.

Zhang, Z., and S. Y. Schwartz (1992), Depth distribution of moment release in underthrusting earthquakes at subduction zones, *J. Geophys. Res.*, *97*, 537–544.

Zobin, V. M., and V. I. Levina (2001), The rupture process of the M_W 7.8 Cape Kronotsky, Kamchatka, earthquake of 5 December 1997 and its relationship to foreshocks and aftershocks, *Bull. Seismol. Soc. Am.*, *91*, 1619–1628.

M. E. Pritchard, Department of Earth and Atmospheric Sciences, Snee Hall, Cornell University, Ithaca, NY 14853, USA. (mp337@cornell.edu)

M. Simons, Seismological Laboratory, Division of Geological and Planetary Sciences, California Institute of Technology, MC 252-21, Pasadena, CA 91125, USA.